

Identifying fault heterogeneity through mapping spatial anomalies in acoustic emission statistics

T. H. W. Goebel,¹ T. W. Becker,¹ D. Schorlemmer,^{1,2} S. Stanchits,^{2,3} C. Sammis,¹ E. Rybacki,² and G. Dresen²

Received 9 August 2011; revised 29 November 2011; accepted 29 November 2011; published 13 March 2012.

[1] Seismicity clusters within fault zones can be connected to the structure, geometric complexity and size of asperities which perturb and intensify the stress field in their periphery. To gain further insight into fault mechanical processes, we study stick-slip sequences in an analog, laboratory setting. Analysis of small scale fracture processes expressed by acoustic emissions (AEs) provide the possibility to investigate how microseismicity is linked to fault heterogeneities and the occurrence of dynamic slip events. The present work connects X-ray computer tomography (CT) scans of faulted rock samples with spatial maps of b values (slope of the frequency-magnitude distribution), seismic moments and event densities. Our current experimental setup facilitates the creation of a series of stick-slips on one fault plane thus allowing us to document how individual stick-slips can change the characteristics of AE event populations in connection to the evolution of the fault structure. We found that geometric asperities identified in CT scan images were connected to regions of low b values, increased event densities and moment release over multiple stick-slip cycles. Our experiments underline several parallels between laboratory findings and studies of crustal seismicity, for example, that asperity regions in lab and field are connected to spatial b value anomalies. These regions appear to play an important role in controlling the nucleation spots of dynamic slip events and crustal earthquakes.

Citation: Goebel, T. H. W., T. W. Becker, D. Schorlemmer, S. Stanchits, C. Sammis, E. Rybacki, and G. Dresen (2012), Identifying fault heterogeneity through mapping spatial anomalies in acoustic emission statistics, *J. Geophys. Res.*, 117, B03310, doi:10.1029/2011JB008763.

1. Introduction

[2] Fault systems contain geometric and structural complexities on multiple scales. The San Andreas fault system, for example, consists of several subparallel faults which accommodate the relative movement of the Pacific and North American plates. The strain accumulation and release in connection with the movement of tectonic plates result in the creation of broad fault zones which evolve over time. The slip distribution along plate boundaries can be explained to first order by geometrically simple systems of planar faults [e.g., Ben-Zion and Sammis, 2003] but the spatial distribution of earthquake hypocenters reveals a picture of great complexity. Seismicity within the continental crust, which is connected to both frictional and fracture processes, is strongly influenced by fault zone geometry, segmentation, and roughness [e.g., Aki, 1979, 1984; Malin *et al.*, 1989;

Zhang *et al.*, 1991; Dietrich and Smith, 2009; Powers and Jordan, 2010].

[3] Within the scope of this study, we investigated the connection between the spatiotemporal distribution of microseismicity and structural heterogeneities of fracture surfaces during laboratory stick-slip experiments. In particular, we concentrated on the influence of geometric fault asperities, which are commonly seen as areas of increased fault strength and resistance to slip. The term asperity has been used in seismological studies to describe highly stressed, locked fault patches. These patches are observed to produce large coseismic moment release during earthquake propagation but can also be linked to rupture nucleation and arrest [e.g., Kanamori and Stewart, 1978; Kato *et al.*, 2010]. In laboratory studies, areas of increased fault strength may be connected to inflections, unbroken asperities, as well as healed or branching faults [e.g., Scholz, 2002; Lei, 2003; Lei *et al.*, 2004; Thompson *et al.*, 2009]. We define asperities as areas of large sliding resistance and more specifically as load-bearing points of contact between rock surfaces [Jaeger and Cook, 1979] as a result, for example, of locally increased positive fault topography. The regions of geometric asperities can be identified using CT scan images and can be connected to episodic locking, enhanced strain accumulation and fault rupture.

¹Department of Earth Sciences, University of Southern California, Los Angeles, California, USA.

²Department of Geodynamics and Geomaterials, German Research Centre for Geosciences, Potsdam, Germany.

³TerraTek A Schlumberger Co., Salt Lake City, Utah, USA.

[4] Fault plane asperities have been studied at crustal and laboratory scales. The latter aim to mimic similar conditions to those inside of the seismogenic crust. An advantage of laboratory experiments is that experimental setups can be adapted to study isolated processes, e.g., the role of an asperity region in creating macroscopic slip events. Rock mechanics experiments have been essential in extending the understanding of physical processes involved in earthquake ruptures. *Brace and Byerlee* [1966] demonstrated that stick-slip during triaxial compression tests of simulated faults may be considered as analogous to earthquakes. Furthermore, the widely used rate and state friction laws were based on laboratory observations [*Dietrich*, 1978; *Ruina*, 1983] and have since been applied to describe parts of complex fault behavior.

1.1. Acoustic Emissions in Laboratory Experiments

[5] Nonelastic deformation of rock specimens in the brittle regime is connected to microcracking events that emit elastic waves similar to seismic waves during crustal earthquakes. The hypocenters and amplitudes of these acoustic emissions (AEs) have been determined with increasingly high accuracy and applied to the description of fracture processes of intact rock [e.g., *Zang et al.*, 1998; *Lei et al.*, 2004]. AEs show a high degree of localization during the initiation of catastrophic failure [*Lockner et al.*, 1991]. *Scholz* [1968] and *Amitrano* [2003] demonstrated that the frequency magnitude distribution (FMD) of AEs during loading of intact samples follows a power law similar to the Gutenberg-Richter distribution of natural seismicity with a decreasing slope (*b* value) with increasing differential stress. *b* values also exhibit a characteristic minimum before the failure of intact rock samples that has been linked to stress-driven micro-crack corrosion and coalescence [e.g., *Main et al.*, 1989; *Meredith et al.*, 1990]. The authors suggest a negative correlation between *b* values and the level of stress.

[6] In addition to fracture experiments, many studies focused on the investigation of naturally and artificially created faults during triaxial compression. *Amitrano and Schmittbuhl* [2002], for example, observed a damage zone containing a gougelayer, as well as regions of high and low crack density during frictional sliding of rough fracture surfaces. A detailed microanalysis showed many mode II cracks that accommodated the fault displacement. *Sammonds and Ohnaka* [1998] conducted experiments on saw-cut faults with predefined roughness which showed that *b* is related to the fractal dimension of the surface topography during frictional sliding with lower *b* values for smoother surfaces. *Thompson et al.* [2009] showed that AE hypocenters during stick-slip on natural fracture surfaces cluster close to asperities. They identified asperities using both CT scan images and AE event locations and suggested that asperity regions in laboratory experiments are analogous to locked patches of crustal faults in that they are barriers to fault slip.

1.2. Spatial *b* Value Mapping

[7] The role of fault zone complexity in the creation of crustal seismicity and its connection to rupture nucleation spots is an area of active research. *Ben-Zion and Sammis* [2003] argued that faults evolve toward geometric simplicity with increasing total offset (“slip age”). The authors suggest geometrical and material heterogeneity of planar

faults as a mechanism that leads to complex seismicity clustering. In subduction zones, fault plane asperities have been identified by high seismic moment release. Corresponding aftershocks are suggested to create areas of high *b* values [*Sobiesiak et al.*, 2007]. The nucleation spots of ruptures have been linked to fault plane asperities, for example for the Parkfield section of the San Andreas Fault [*Schorlemmer and Wiemer*, 2005]. An investigation of spatial *b* value variations along the Parkfield section revealed a pronounced low *b* value anomaly that coincides with a fault plane asperity [*Wiemer and Wyss*, 1997; *Schorlemmer et al.*, 2004]. This area produced also large coseismic slip during the 2004 $M = 6.0$ Parkfield earthquake [*Schorlemmer and Wiemer*, 2005]. A detailed mapping of fault plane asperities could play an important role in seismic hazard assessment. While variations in seismic *b* values have been associated with asperities in natural faults there is a lack of additional data to validate this interpretation. The physical mechanisms involved in their creation remain unclear, for example, if low *b* values are a consequence of regional fault criticality, or the failure of one or more large asperities on a rough fault.

[8] We extend previous studies by connecting detailed *b* value maps with in situ fault structure observations. While many laboratory experiments were focused on the mechanism of rock fracture, we put our emphasis on the analysis of AEs during stick-slip sliding. We created naturally faulted surfaces and observed the AE build up with approaching dynamic slip events as well as AEs occurring immediately after slips. AE events can be related to both fault morphology and branching [e.g., *Lei et al.*, 2004; *Thompson et al.*, 2009]. AE hypocenter locations and amplitudes were analyzed within the framework of a single fault zone, thus isolating the influence of asperities from other suggested geometrical heterogeneities like fault branching. We developed a method to create several stick-slips on one fault to test the persistence of major asperities.

[9] AE patterns were related to fault heterogeneities as revealed by CT scan images and microstructural analysis. In this study, results from three stick-slip experiments are presented. Initially, we describe the mechanical details of fault creation and the following stick-slip events. We then show the applicability of concepts and statistical relations derived from crustal seismicity to our data, namely to the microseismicity which occurred in connection with stick-slips. The main part of this study is focused on the identification of fault plane asperities using *b* values, seismic moment release, and event densities of AEs, and to compare it to CT scans. Lastly we look at the evolution of the fault plane structure with successive stick-slip events.

2. Method

2.1. Rock Sample and Loading

[10] We present results from triaxial compression experiments conducted on three, cylindrical (40 × 107 mm) Westerly granite (WG) specimens. Westerly granite, which is a good representative of the continental, seismogenic crust, is isotropic and consists of 28% quartz, 33% plagioclase, 33% K-feldspar, 5% mica (3.5% biotite, 1.9% muscovite) [*Chayes*, 1950] with an average grain size of 0.75 mm [*Stesky*, 1978].

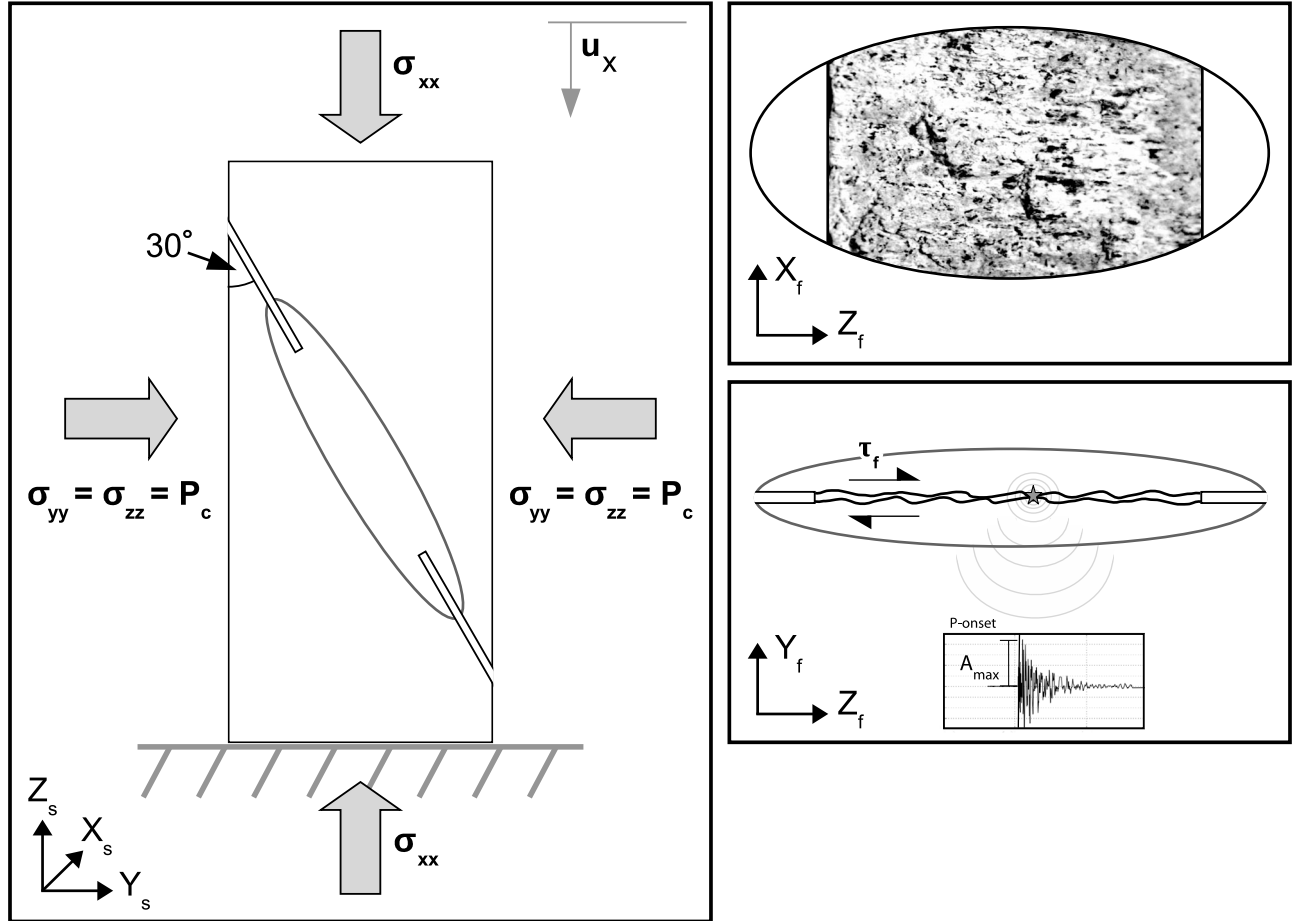


Figure 1. (left) Schematic diagram of loading conditions and stresses. Arrows at bottom left specify the sample-specific coordinate system. (right) Sliding of fault with naturally developed roughness in fault specific coordinate system which is also used for the later AE representation.

[11] Rock fracture and frictional sliding were performed with a 4600 kN MTS servo-controlled loading frame and a 200 MPa pressure vessel. All experiments were conducted on previously oven dried samples to avoid additional complexity and to facilitate the interpretation of results. An elastic rubber jacket was installed around the specimens to prevent any fluid penetration during the experiments. The axial force was measured by an external load cell. Both vertical and horizontal strain were determined by local strain gauges and larger scale deformation braces (similar to LVDTs). The maximum displacement, which was limited by the strength of the rubber jacket, was ~ 6 mm depending on the experimental set up and rock sample preparation. We used piezoceramic sensors with 1 mm thickness and a resonance frequency of 2 MHz for AE recording and ultrasonic pulse generation. Samples were drilled from homogeneous granite blocks, without any visible cracks. The end surfaces were cut and ground parallel to ± 0.03 – 0.1 mm. For specimens WGRN04 and WGRN05, we introduced saw-cut notches in a 30° angle to the loading axis on opposite sides of the samples. An approximately 1 mm wide gap was created due to the thickness of the cutting disc which was filled with low friction teflon sheets. The notches provided a guide for fracture propagation resulting in the localization of deformation between their ends.

[12] Post experimental microanalysis of fault structure and crack network was performed using a X-ray computer tomography system (GE Phoenix X-ray nanotom 180 NF) equipped with a 180 kV/15 W nanofocus tube and a digital 5 Megapixel detector. The theoretical resolution of CT scans is ~ 30 μ m, but in practice the resolution decreases due to boundary effects, small density contrasts between different grains and limited penetration for large sample sizes. Scanning of samples by X-rays allows visualizing density contrasts on gray-scale images because the absorption of the electromagnetic waves depend on material contrasts (density, atomic number), thickness, and radiated X-ray energy.

2.2. Fracture of Intact Rock and Stick-Slip Events on Fault

[13] We developed a three-step procedure, in which initially the intact part of the rock samples were fractured during axial loading at constant strain rates of $\dot{\epsilon} \sim 3 \cdot 10^{-6}$ s $^{-1}$ (20 μ m/min) and confining pressure of $P_c = 75$ MPa (Figure 1, left). As a second step, we locked the fault by an increase in confining pressure to 150 MPa and during the final step resumed axial loading which led to a reactivation of the fault (Figure 1, right) in form of a series of stick-slip events. The uncertainty in stress, confining pressure and displacement were estimated to be 6 MPa, 0.5 MPa and

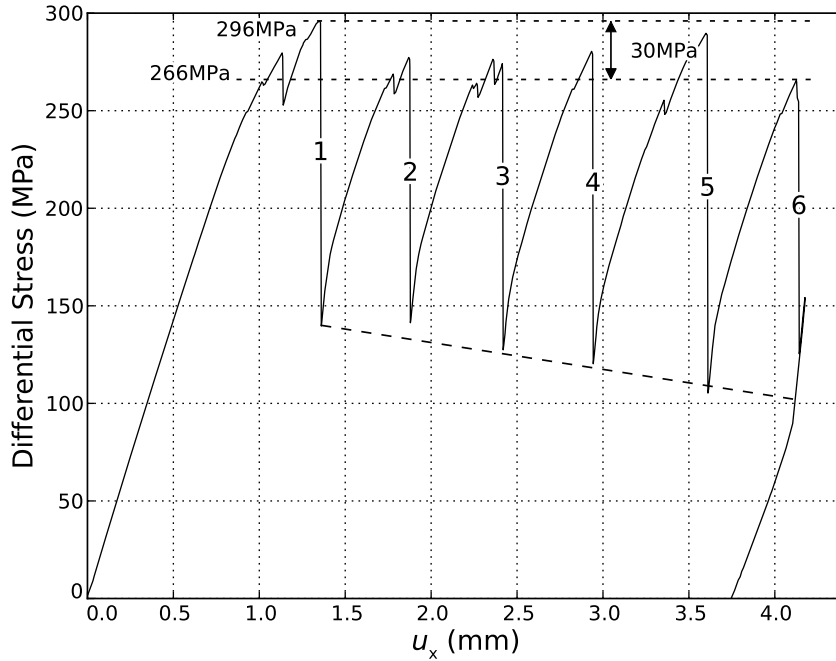


Figure 2. Differential stress and axial displacement (u_x) for experiment WGRN05 with characteristic stick-slip behavior. The slip events with large stress drops are labeled from 1 to 6. All slip events with large stress drops nucleated within a differential-stress window of 30 MPa (dashed lines at top). The residual stress decreased systematically after each successive stick-slip as indicated by the downward sloping dashed line.

3 μm respectively. Initial experiments were conducted on completely intact samples followed by a later set of experiments on notched specimens. The failure process of intact samples from our earlier experiments (not shown) resulted in complex fault structures that contained multiple fracture surfaces. The introduction of notches provided a key improvement in our experimental setup and ensured the reproducibility of results. The naturally developed laboratory faults had a simpler structure and a single fault plane with predictable orientation. This information could be used to optimize the locations of AE sensors on the sample periphery.

[14] Figure 2 shows the loading curve during fault activation of WGRN05 with characteristic stick-slip behavior. We observed an initial linear increase of stress and strain which was followed by a growing deviation from linearity leading up to stress drop events which were connected to macroscopic slip of the entire fault. Six abrupt slip events with stress drops ($\Delta\sigma$) between 132–181 MPa and duration of max. 0.1 s were observed during frictional sliding of

sample WGRN05 (Figure 2). All slip events occurred within a differential stress window of 30 MPa between peak stresses of 266–296 MPa without any systematic changes in the maximum fault strength. The largest stress drop was connected to slip event 5. The residual stress after each of the slips decreased systematically (downward sloping, dashed line in Figure 2), which is likely to be connected to fault smoothing with successive slip events.

[15] Table 1 shows loading conditions and number of slip events for the three different samples that were used in this study. The specimen WGR01 had no notches but a through-going fracture surface with natural roughness and a coefficient of friction of about 0.66. It produced one slip event with a large stress drop. This stress drop was preceded by about 60 min of frictional sliding at a consistently high differential stress level which was interrupted by several smaller slips. The notched samples, WGRN04 and WGRN05, produced three and six stick-slip events, respectively, with stress drops between 115–217 MPa. The maximum differential stress during fracture and sliding phases decreased from

Table 1. Overview of Experiments and Boundary Conditions Conducted on Samples WGR01, WGRN04, and WGRN05^a

Slip Event	Sample	l_{rs} (cm)	l_n (cm)	$P_{c_{frac}}$ (MPa)	$P_{c_{slide}}$ (MPa)	$\sigma_{max_{frac}}$ (MPa)	$\sigma_{max_{slide}}$ (MPa)	$u_{x_{max}}$ (mm)	N_{slips}
1	WGR01	8.5 ± 0.15	—	75 ± 0.5	150 ± 0.5	780 ± 6	570 ± 6	3.1	1
2	WGRN04	5 ± 0.15	1.5 ± 0.15	75 ± 0.5	150 ± 0.5	610 ± 6	400 ± 6	3.0	3
3	WGRN05	4.2 ± 0.15	1.9 ± 0.15	75 ± 0.5	150 ± 0.5	505 ± 6	295 ± 6	4.1	6

^aWGR01 was fractured in its intact condition while WGRN04 and WGRN05 contained notches. l_{rs} , approximate length of the rough fracture surface; l_n , length of each notch; $P_{c_{frac}}$, confining pressure during fracture stage; $P_{c_{slide}}$, confining pressure during frictional sliding of the fractured surfaces; $\sigma_{max_{frac}}$, maximal differential stress during fracture stage; $\sigma_{max_{slide}}$, maximal differential stress during sliding; $u_{x_{max}}$, maximum vertical displacement; N_{slips} , number of abrupt slip events with large stress drops.

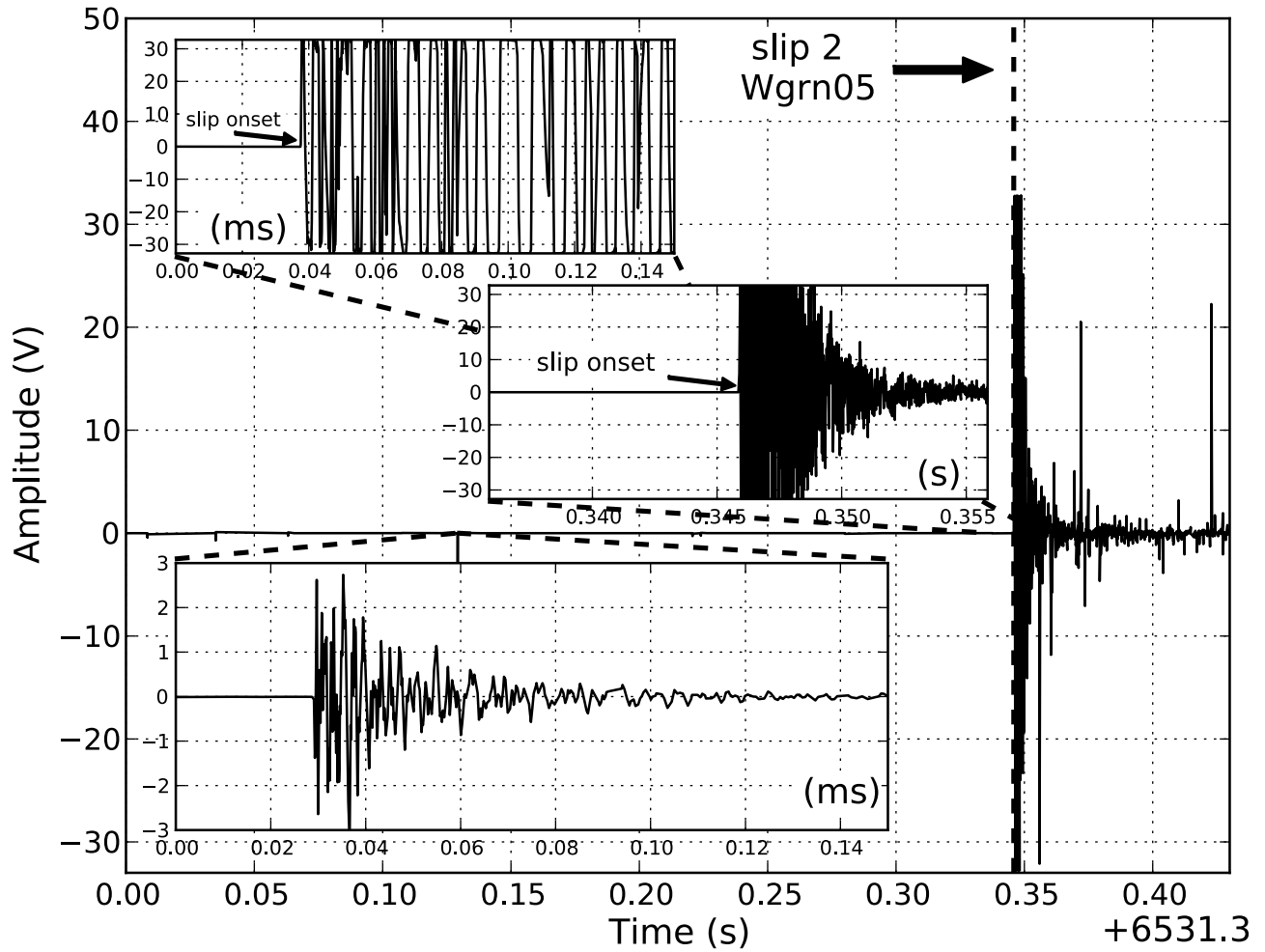


Figure 3. AE waveforms within a ~ 0.5 s (main axis), 20 ms (middle) and 0.15 ms (inset at top) time window of slip event 2 of experiment WGRN05 as well as a waveform of a “typical” AE event (inset at bottom). The waveforms connected to slip onsets were clearly distinguishable from commonly observed AEs by their amplitude and duration. Note that time scales are in ms for the top and bottom insets.

WGR01 to WGRN05 as a result of specimen weakening due to longer notches. The maximum axial displacement was between 3.0 and 4.1 mm.

2.3. AE Data

[16] The main focus of this study was to connect AE properties (namely magnitude, density, b value, and location) to specific heterogeneities of the fault zone. We recorded and analyzed complete acoustic emission waveforms from 16 piezoceramic transducers with a resonance frequency of about 2 MHz using eight high-speed digitizer cards with 80 GByte internal hard disk space. The internal hard drives prevent any type of data loss due to downtime during streaming. Each channel was operated in a triggered mode at a sampling frequency of 10 MHz (corresponding to a time resolution of $0.1 \mu\text{s}$) and an amplitude resolution of 16 bits. Large deformation during fracture and shear caused significant changes in elastic moduli, hence also in seismic velocities. To account for these variations during hypocenter determination, velocities were computed every 5 to 30 s from onset times of high-voltage pulses transmitted by piezoceramic sensors. This technique improved the location

accuracy to about 1–4 mm. Further details about the AE system are given by Stanchits *et al.* [2006].

[17] The amplitude of each AE event was determined similarly to Zang *et al.* [1998]:

$$A = \sqrt{\frac{1}{k} \sum_{i=1}^k \left(\frac{r_i}{10} A_{i,\max} \right)^2} \quad (1)$$

where $A_{i,\max}$ is the maximum amplitude of the AE waveform at each sensor, r_i is the distance between the source and the i th receiver in millimeter and k is the total number of sensors used for the amplitude calculation. The computed value is an average amplitude for the whole array assuming elastically propagating, spherical waves of a point source, corrected for geometrical spreading on a 10 mm reference sphere.

[18] Within the framework of this study we distinguished between AEs which were described by their locations, magnitudes, and origin times and macroscopic, dynamic slip events with specific stress drops, durations, and onsets of stress drops. Dynamic slip events were associated with a whole set of AE events, consisting of AE “foreshocks,”

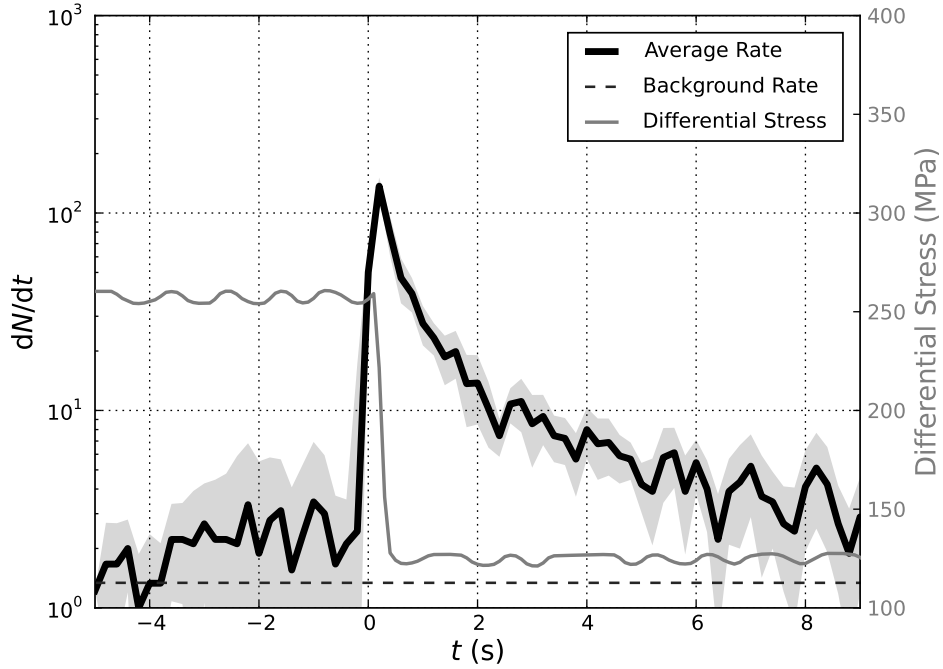


Figure 4. Differential stress (gray line), AE rate average (black line), standard deviation (shaded gray region), and background rate (dashed gray line) for all slip events of WGR01, WGRN04 and WGRN05 within a 15 s time window of slip onsets, stacked to $t = 0$. The origin times of slip events were determined from the stress drop onsets and compared to AE data. The highest AE rates occurred within less than $100 \mu\text{s}$ of the stress drops.

“main shocks” and “aftershocks.” The nucleation spots of macroscopic slip events were defined as “main shocks.” They were easily detectable due to abrupt increases in AE rates, their temporal proximity to the onsets of large stress drops, their distinct waveforms as well as their large amplitudes. An initial main shock selection was performed by identifying the largest magnitude AE within a 0.2 s time window around the onset of stress drops. This time window accounts for the different sampling rates and synchronization uncertainties of AE and stress data. The main shock identification was then confirmed by analyzing the waveforms associated with slip onsets and by comparing them to a waveform of a typical AE event. The two signals showed very distinct characteristics (Figure 3) in terms of duration and amplitude. A commonly observed AE event exhibits a burst signal of high frequency, with high, initial amplitudes which decay rapidly within less than 0.050 ms. AE waveforms of slip events generally show larger amplitudes that are clipped on all channels due to the limited dynamic recording range of the AE system. The signal can have a total duration of up to 10 ms. Right after the sliding, several aftershock AEs might be hidden in the coda of the large event, for which recordings were momentarily clipped by the large signal, as is common for actual earthquake studies. However, this temporary loss of recording ability did not affect our statistical studies or the identification of the main shocks.

[19] In the context of a main shock, we then defined aftershocks as AE events in an 8 s time window after the origin time of the main shock. Foreshocks were defined as AEs that occurred from 20 s after the previous slip until 0.2 s before the current slip event. For the spatial analysis of

foreshocks, we selected AEs with larger magnitudes and small residuals from the travel time inversion of the location algorithm to ensure the highest possible accuracy of hypocenter determination. We decided to choose a sufficiently small aftershock period to avoid any mixing of different event populations. Figure 4 shows an example of the AE activity binned to 0.1 s before and after the origin time of macroscopic slip. The AE rates right before the slip events were low compared to aftershock rates. The onsets of stress drops coincided with a sharp peak in AE rates (within sampling accuracy of 0.1 s for stress and AE rate). We observed a rate decrease with time after slip until it reached approximately preslip rates.

[20] Based on AE amplitudes, we assigned magnitudes ($M = \log A$) to each event on an experiment-specific scale and seismic moments using

$$M_0 = 10^{CM}. \quad (2)$$

Here, we chose $C = 3/2$ which is commonly used for real earthquake scaling relationships. Our analysis focused on relative, spatial variations in M_0 which is why changes in C cause only an up or down scaling but have no influence on the detectability of spatial variations. Both magnitude and seismic moment were computed on an experiment-specific reference scale.

[21] Frequency-magnitude distributions of AE events follow a power law of the form

$$\log N = a - bM \quad (3)$$

where b is the slope of the number of events (N) vs. magnitude (M) and a provides an estimate for the productivity

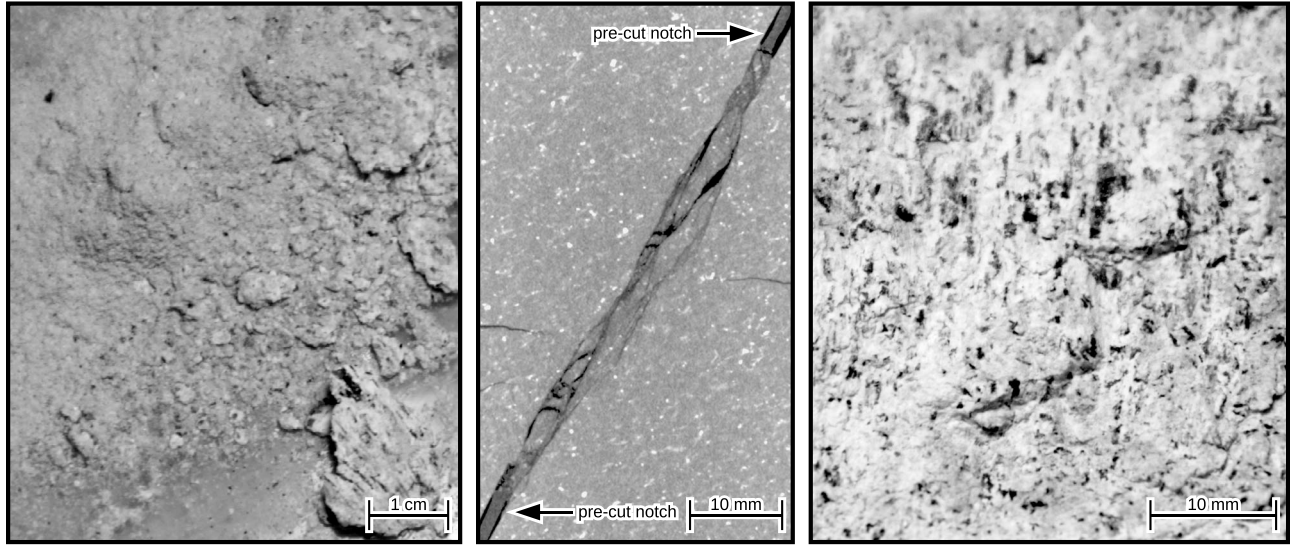


Figure 5. (left) Photo of gouge, which was produced within the fault zone during the 6 stick slips of WGRN05, consisting of ultrafine and larger grains. Larger rock flag at bottom right shows evidence of slickensides and black elongated grains as a result of slip under high normal stress. (middle) CT image of the fault structure with scale in mm after the completion of the experiments. The fault width and gouge layer thickness varied along the fault. (right) Photo of fault surface with many slip-parallel slickensides and topographic relief changes of up to 2 mm.

analogous to the *Gutenberg and Richter* [1944] relationship. To compute b values, we use the maximum likelihood approach [Aki, 1965].

$$b = \frac{1}{\bar{M} - M_c} \log(e) \quad (4)$$

where M_c is the magnitude of completeness estimated by the maximum curvature of the distribution, corrected for bin size [Utsu, 1965; Guo and Ogata, 1997] and \bar{M} is the mean magnitude. For a reliable b value estimate we required distributions to contain at least 150 AEs.

[22] We performed a detailed analysis of spatial AE clusters by first projecting all AEs into the fault coordinate system using the best fit fault plane vectors which are the eigenvectors of the covariance matrix of AE locations obtained by singular value decomposition. We then computed b value, AE event density, and moment release maps based on events in the proximity of the fault plane by creating a 2D grid with 0.1 mm node spacing. We determined b for frequency-magnitude distributions for the N (with $N \geq 150$) closest AEs to each node within a maximum radius of $r_{\max} = 7$ mm or $r_{\max} = 10$ mm, respectively, depending on the overall AE activity in a specific foreshock time window. This method provides an optimized resolution for b value estimates while accounting for a changing AE event density in different parts of the fault. Nevertheless, each b value still represents a volume rather than one specific point on the fault surface.

[23] We computed the seismic moment release per volume (M_0/V) between slip events by summing the seismic moment within spheres of constant radius centered at fault plane nodes. AE event density (ϕ) maps were created by counting events within spherical subvolumes of the fault plane which

were then corrected for volume size and length of the time windows of foreshock and aftershock occurrences.

3. Results

3.1. Fault Topography and Microstructure

[24] Post experimental inspection of the samples showed areas of complex fault structure consisting of gouge, a damage zone containing microcracks with varying density, and the host rock which was characterized by little damage. The initial grain size distribution after fracturing decreased substantially during frictional sliding due to comminution, leading to the creation of large amounts of ultrafine rock powder. The combination of grain comminution and the localized occurrences of AE events close to the central fault plane as well as the decrease of the residual friction with progressive stick slips suggested an ongoing reshaping of the fault surface. The successive stick-slip events lead to an accumulation of fine-grained gouge on the fault surfaces (Figure 5, left) as a result of asperity grinding and grain size reduction. We observed both highly fractured fine grained gouge and individual larger rock particles that were produced through the propagation of larger cracks into the host rock. Different grain sizes may be an expression of different stages of damage evolution.

[25] We performed a CT scan of sample WGRN05 after experiment completion which revealed a heterogeneous fault structure with different size cracks between the ends of the notches. We identified a fault zone with one or possibly several through going fault surfaces that accommodated the macroscopic slip. Several subsets of cracks formed a zone of highly fractured rock of variable thickness (Figure 5, middle). This zone was up to ~ 1 cm wide. We observed an anomalously thin part of the fault zone towards the center

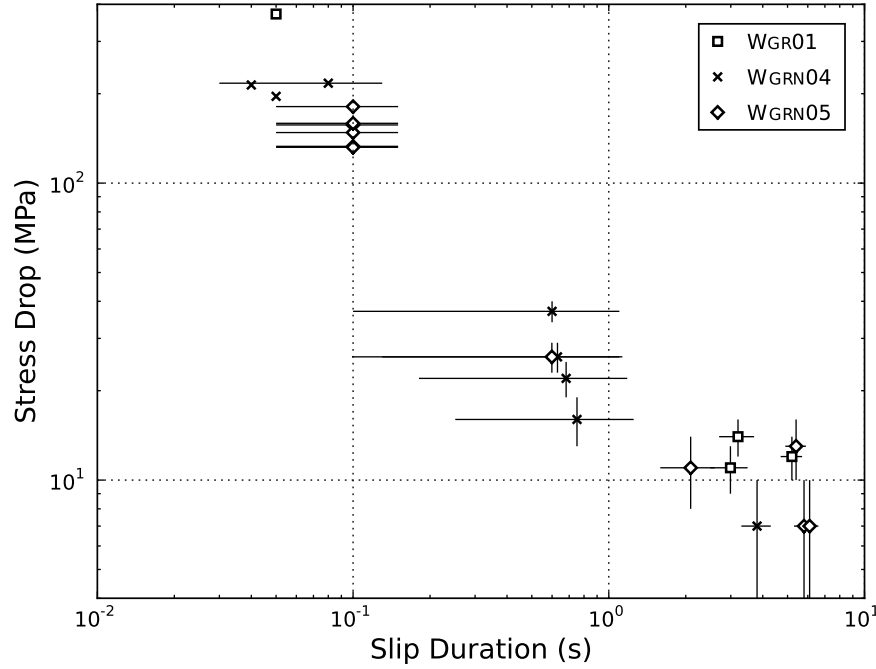


Figure 6. Stress drop ($\Delta\sigma$) and duration of slip events for three different samples. Vertical errors represent uncertainties in stress measurements while horizontal uncertainties are estimated errors for onset picks of stress drop start and end which are larger for small stress drops due to a smaller signal to noise ratio. Slip events with large stress drop had a maximum duration of 0.1 s. Decreasing stress drops were connected to increasing slip durations of up to 6 s. The duration uncertainty for all large stress drops was 0.1 s while low stress drop events had estimated uncertainties of 0.5 s.

of the sample. This area could have led to episodic fault locking and enhanced microcracking in the vicinity due to stress intensification. Visual inspection of fault topography after the experiments (Figure 5, right) supports the theory of the existence of large asperities on the fault surface: several areas of increased roughness and larger relief changes were observed forming points of contact between the two host rock surfaces of the sample. Despite the complex fault structure, we observed many slip-parallel slickensides of up to 0.5 cm length. Slickensides in laboratory experiments are connected to dynamic slip events [Engelder, 1974] and are also encountered in exhumed, natural faults.

3.2. Stress Drop and Duration

[26] The loading curves of our sliding experiments showed sudden slips with large stress drops in addition to many smaller slip events with varying stress drops. We investigated the connection between stress drops and duration of macroscopic slip events by compiling data from samples WGR01, WGRN04 and WGRN05 (Figure 6). The confining pressure for all three rock specimen was 150 MPa but in contrast to WGRN04, and WGRN05, WGR01 did not contain any notches. The sliding experiment of WGR01 was dominated by an extended period of high differential stresses with relatively small stress changes of ~ 20 MPa. We observed several small slips that may have prepared the fault for the large slip event which occurred after ~ 60 min. Experiments performed on WGRN04 and WGRN05 produced slip events in a systematic fashion without extended preparatory periods. For all three specimens, we observed

two different groups of slip events: (1) slips with $\Delta\sigma \gtrsim 130$ MPa which were always abrupt with max. durations of less than 0.1 s, (2) low stress drop events ($\Delta\sigma \lesssim 50$ MPa) with longer durations. The slip events with largest stress drops exhibited also sudden onsets and the shortest durations. Small stress drop events showed longest duration of up to 6 s. (The accuracy of the duration of large stress drop events was limited by the sampling rate of the load cell so that all values between 0.06–0.1 s could be seen as upper limits.) Abrupt and slower slip events occurred at similar stress levels. This emphasizes that not only the far-field stress levels determine the onsets of slip events but also geometric fault heterogeneities may have an important influence on the locations of rupture nucleation points and times.

3.3. Aftershock Rates and Locations

[27] We computed AE rates by summing events in 0.1 s bins for a 5 second period after each slip event. Figure 7 shows aftershocks after slip event 2 and 5 of WGRN05 in linear and logarithmic scale as an example of a typical rate decay after slips. The AE rate decreased rapidly for the first 0.2–1 s followed by a more gradual decrease over several seconds until reaching the preslip rates. To quantify this behavior we use the Omori-Utsu law [Utsu, 1962] which captures both a power law decay and an initial period for which the rate is lower than predicted by a power law:

$$\frac{dN}{dt} = \frac{K}{(c + t)^p} \quad (5)$$

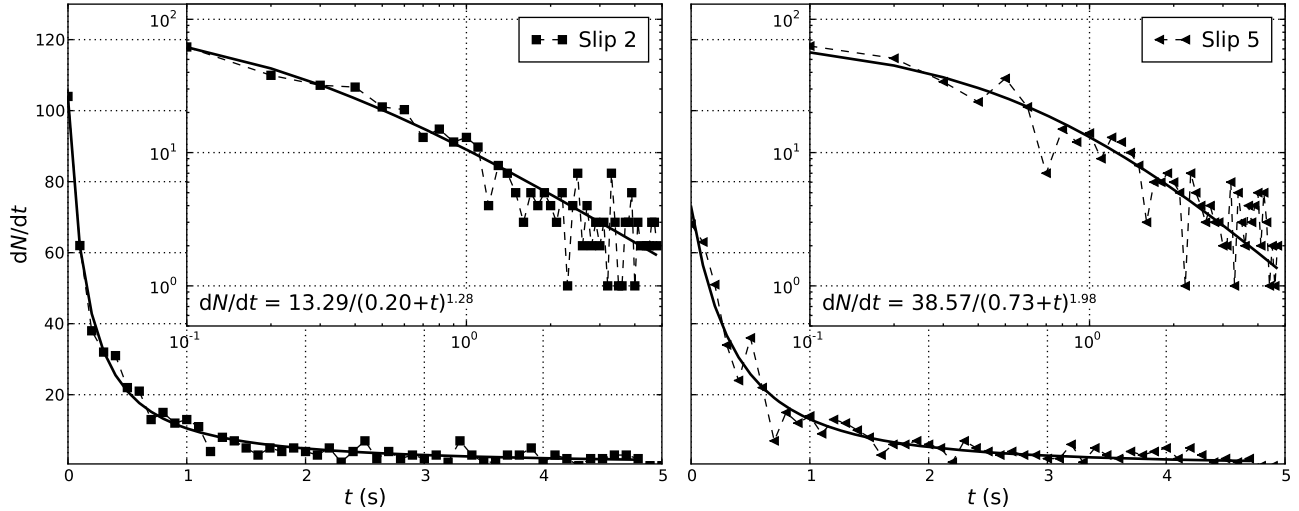


Figure 7. AE aftershock rates for slip events 2 and 5 plotted in linear and logarithmic scale.

where $\frac{dN}{dt}$ is the aftershock rate and t is the time after slip. K , c , and p are empirical fitting parameters. K is related to the productivity of the aftershock sequence, c describes the length of the time window of initial deviation from power law decay and p is the rate decay exponent. Slip event 2 of WGRN05 had a significantly shorter period of deviation from the power law compared to slip event 5 resulting in a smaller c value. The overall productivity and rate of decay was higher for aftershocks of slip 5.

[28] Table 2 shows results from the analysis of the aftershock rates of all slip events of WGRN04 and WGRN05. WGRN04 showed p values close to unity except for slip 3 where we observed a high p value of 1.21. c values varied between 0.19 and 0.34 and K values changes between 15.71 and 20.11. The observed activity, N_{tot} , and peak rate, $(\frac{dN}{dt}(t = 0))$ right after slip event occurrence decreased for each successive slip event of WGRN04.

[29] The decay rate p and delay time c for specimen WGRN05 decreased systematically from slip event 1–6 except for slip event 5 which was connected to anomalously high parameters in the Omori-Utsu law. The recorded number of AEs within the aftershock sequence 5, N_{tot} , exceeded the two preceding ones despite exhibiting a comparably low initial AE rate, $(\frac{dN}{dt}(t = 0))$. Small $\frac{dN}{dt}(t = 0)$ and high Omori-Utsu parameters for aftershock sequence 5 could be an indication of a large amount of small events that were not recorded during the period right after the slip onset which would explain high K values despite lower observed activity N_{tot} . Slip event 5 produced also the largest stress drop of all events possibly connected to a change in fault roughness, e.g., due to the fracture of a large asperity. Hence both mechanical and AE aftershock data could be explained by the failure of a fault asperity. There are strong trade-offs between the parameters of the Omori-Utsu law and $\frac{dN}{dt}(t = 0)$ (and hence K , given c and p) is difficult to estimate. If we fix c to 0.2, for example, the trend in textit{p} is less clear. We leave statistical exploration of significance to a latter stage when more experiments are available.

[30] Figure 8 shows the locations of main shocks and aftershocks for the three slip events of WGRN04 and the six

slip events of WGRN05 in the fault coordinate system. Hypocenter locations were projected onto the fault plane and are viewed, looking onto the fault plane (Figure 8, top) and looking at a side view of the fault plane (Figure 8, bottom). The AE activity was very low within 0.1 s after the main shock occurrence possibly due to events that were hidden within the main shock coda. Thus the nucleation spot of a macroscopic slip event (red stars in Figure 8) could simply be defined as the hypocenter location of the largest amplitude event during that 0.1 s time frame. The main shocks were clustered between $[Z_f = 46, X_f = -7]$ and $[54, 6]$ in a $\sim 0.5 \text{ cm}^3$ volume for WGRN04 and $[44, -4]$ and $[53, 5]$ in a $\sim 1.5 \text{ cm}^3$ volume for WGRN05 close to the fault plane. Slip event 2 of WGRN05, which nucleated in the lower part of the sample, formed an exception. Common nucleation spots of macroscopic slips could indicate a common mechanism for their creation, for example the rupture of strong fault plane heterogeneities or areas with increased roughness. The aftershocks in both experiments occurred throughout the sample with a small degree of localization on the fault plane. This could be caused by enhanced micro-cracking during strain release and lower differential stresses

Table 2. Parameters K , c , p of Omori Law Fit for Slip Events of Experiments WGRN04 and WGRN05^a

Slip Event	K	c	p	N_{tot}	N_0
<i>WGRN04</i>					
1	20.11 ± 0.64	0.20 ± 0.02	1.09 ± 0.05	751	114
2	15.71 ± 0.63	0.19 ± 0.02	1.01 ± 0.06	590	87
3	19.01 ± 1.61	0.34 ± 0.05	1.21 ± 0.10	550	68
<i>WGRN05</i>					
1	21.11 ± 1.27	0.32 ± 0.03	1.53 ± 0.09	655	116
2	13.29 ± 0.57	0.20 ± 0.02	1.28 ± 0.08	542	104
3	10.61 ± 0.50	0.18 ± 0.03	1.24 ± 0.09	492	86
4	13.44 ± 0.53	0.17 ± 0.02	1.10 ± 0.07	505	94
5	38.57 ± 10.8	0.73 ± 0.13	1.98 ± 0.23	518	68
6	14.97 ± 0.45	0.15 ± 0.01	1.10 ± 0.05	609	122

^a c is in seconds and both N_{tot} and N_0 number of events. N_{tot} is the total number of events within an aftershock sequence and N_0 is the initial and also maximum number of events within an aftershock sequence.

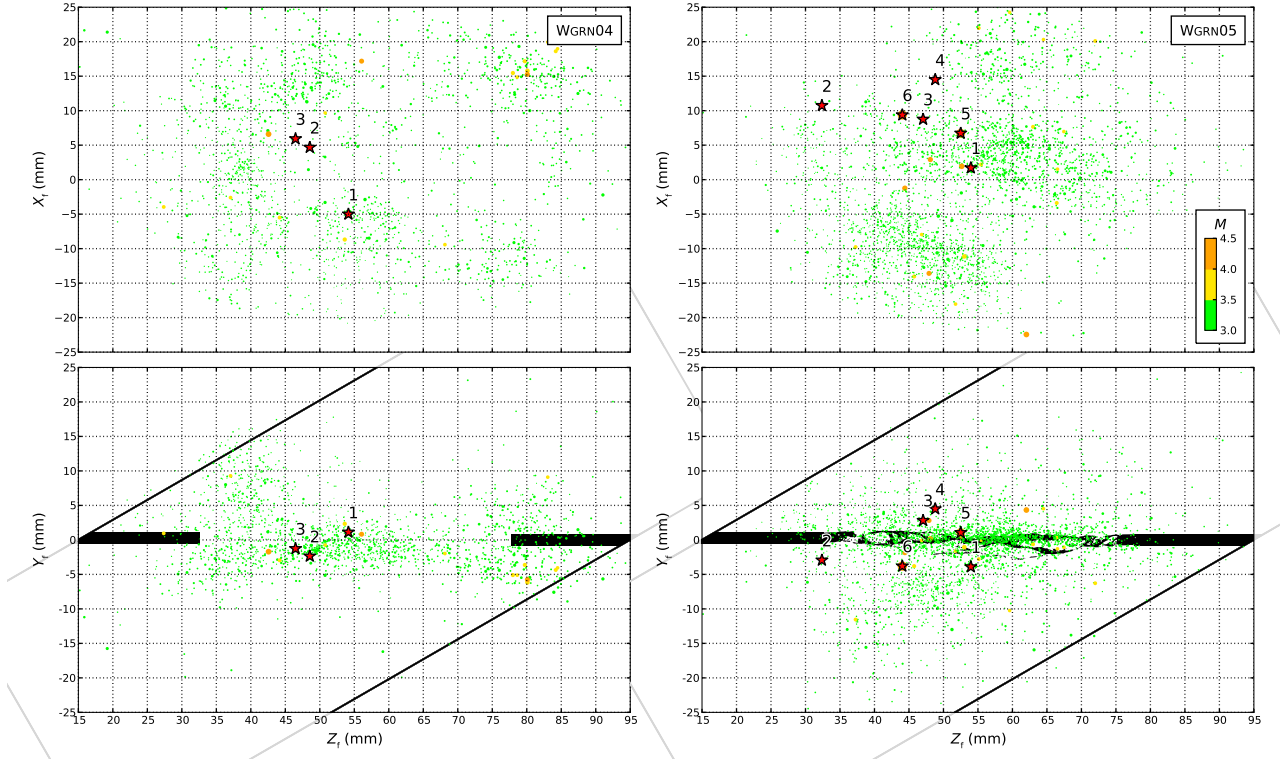


Figure 8. Figure 8 (top) shows AEs (main shocks and aftershocks) projected onto fault plane; Figure 8 (bottom) images AEs within a plane normal to the fault for samples (left) WGRN04 and (right) WGRN05. The red stars indicate the location of the large amplitude AEs coinciding with the onset of the stress drops for all slip events. Dots are aftershocks to slip events colored with size. The nucleation points of stick-slips cluster within similar regions for individual experiments except for event 2 of WGRN05.

after slip events. The following section will focus on a detailed analysis of fault geometry and its changes with successive slip events of WGRN05 and WGRN04.

3.4. AE-Based Asperity Detection

[31] We now concentrate on the identification of larger-scale asperities and their role during the nucleation process of the six slip events of WGRN05. We analyzed the spatial distribution of foreshock behavior preceding slip events of WGRN04 and WGRN05. One prominent feature of the spatial distribution of foreshocks was an abrupt change from high to low activity which was observed within the same area over multiple slip events. Figure 9 shows an example of the foreshock activity to slip event 1 and 2 of WGRN05 which changed from high at $[Z_f = 55, X_f = 3]$, to almost no at $[52, 5]$ to little activity at $[45, 5]$ along the Z_f axis. The variation in AE activity could be a result of different fault-plane roughness along this path. The activity contrast is likely to be connected to an asperity region highlighted by a red circle in Figure 9. Large magnitude foreshocks nucleated close to the asperity boundaries, probably due to crack initiation and growth in preparation of asperity failure. The main shocks of slips 1, 3, 4, and 6 were located close to an activity “gap” region. The asperity seemed to control the nucleation spots of most slip events so that during locked periods large foreshocks nucleated predominately in its proximity.

3.5. Mapping b Values, AE Event Density, and Moment Release

[32] Figure 10 shows the AE event density, b value, and moment release for the foreshocks of slip 1 of WGRN05. The foreshocks were clustered within several areas with elevated event densities. Largest AE event densities were measured at $[Z_f = 37, X_f = 8]$, $[62, 3]$, and $[72, -2]$. The large heterogeneity of AE densities points towards the existence of a few, larger-scale asperities which caused AEs to cluster in their proximity. One area of anomalously low b values was located about 5 mm to the left of the high event density region $[42, 7]$ and a second low b values area was located at $[56, 5]$. The center of the previously identified asperity region was located between these two regions. To emphasize differences in b values we compared the frequency-magnitude distributions (FMD) of AEs within and outside of the asperity (Figure 10 (middle), bottom left). The FMD for AEs connected to the asperity contained relatively more large-magnitude events which caused the large difference of ~ 0.5 in b values. The main shock occurred well within a zone of low b value. Similarly to the event density and b value maps, the moment release was dominated by two main areas centered at $[45, 7]$ and $[56, 5]$.

[33] To investigate if low b value regions and high event densities were always located close to the asperity and to determine the corresponding relative locations of the slip

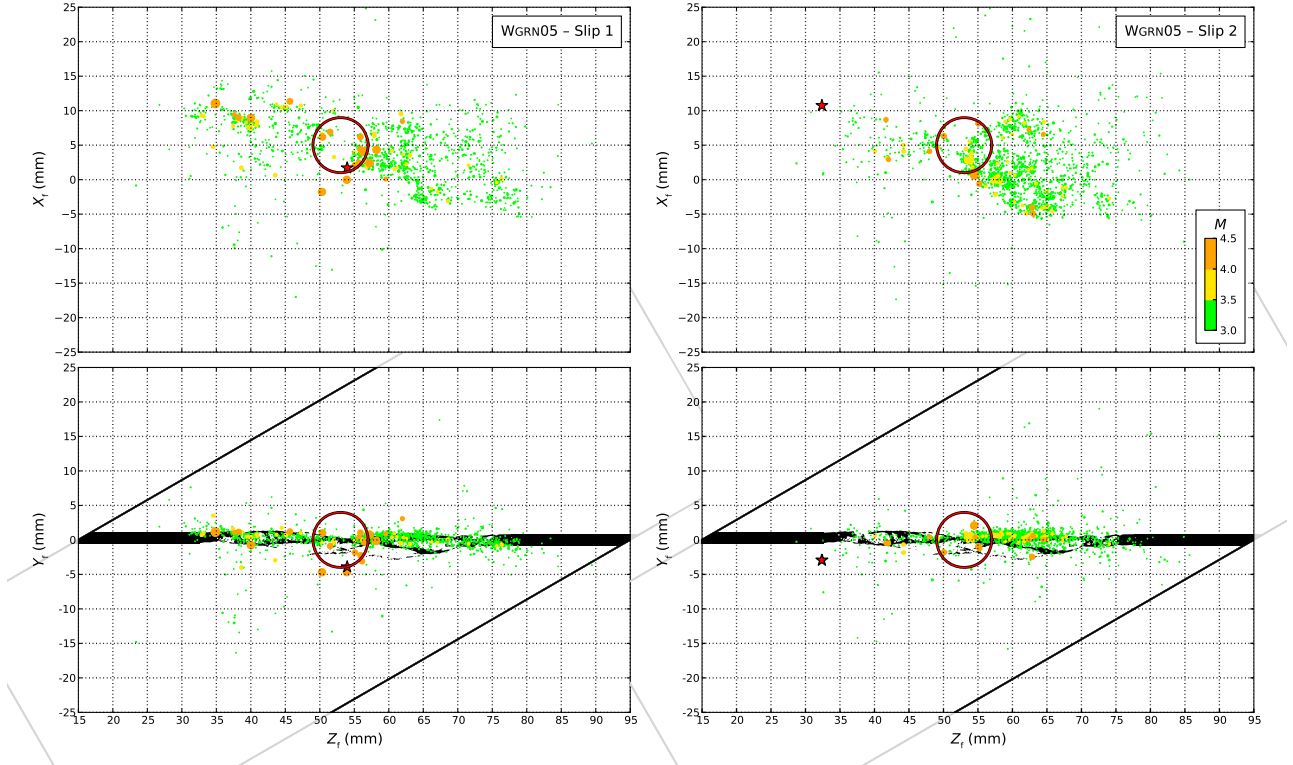


Figure 9. Examples of AE foreshock activity based on slip events 1 and 2 of WGRN05. The red circle highlights an area of a relatively sharp contrast between low and high AE activity. Many large amplitude events were produced in the periphery of this area before each of the slip events.

nucleation points, we performed a spatial b value mapping for foreshocks of all six slips of WGRN05 and plotted the contour lines of the mean AE densities for each slip event (see Figure 11 for examples of b value maps for slip event 2, 3, and 5 of WGRN05). The nucleation points of 5 out of the 6 slip events of WGRN05 were within an area of low b values. For the first three slip events the highest foreshock and aftershock densities were centered at similar points just to the right of the asperity. Aftershock locations started to deviate from foreshock locations after slip event 3. Areas of high aftershock densities still seemed to border low b value regions but were now shifted to the lower left, centered at [45, -8]. The asperity region (red circle in Figure 11) can be identified through combining information of event density and b value maps. An overlap between high foreshock densities and low b values, bordering high aftershock densities, was an indicator for the location of an asperity region close by. High aftershock densities seemed to occur at its outer edges. These observations underline that the asperity caused relatively larger-magnitude AEs to nucleate at its boundaries, creating areas of relatively lower b values and elevated foreshock and aftershock densities.

[34] Figure 12 shows AE event densities and b values for WGRN04. The aftershocks following slip 1 exhibited highest densities above and below a region with several relatively low b values of less than 0.74. We identified an asperity region by applying similar criteria (a combination of low b value, increased moment release, and event density) as for WGRN05. These areas were characterized by low b

values and an abrupt change from low to high foreshock activity. Initially, we observed about four different low b value anomalies on the fault plane which suggested several candidate regions that met our asperity criteria. The decrease in complexity of b value maps after the first slip enabled the identification of one specific asperity centered at [50, 4]. The highest foreshock and aftershock densities (centered at [55, -8], [47, 15] for slip 1, [55, -8], [38, 0], [40, 0], [45, 5], for slip 2, and [55, -8], [42, -12], [40, -3], [40, 5], [50, 15] for slip event 3) were located around the asperity. Again, the highest foreshock and aftershock densities occurred in different fault regions indicating a shift in activity as a consequence of stress transfer between some areas of the fault plane during slip.

[35] To provide information on the location of asperities, AE event-density maps image the degree of clustering of seismic activity within certain time frames of a particular experiment. Figures 11 and 12 show contours of the mean densities before (solid contour lines) and after (dashed contour lines) the slip events of WGRN04 and WGRN05. The foreshock densities of WGRN04 showed a larger spatial variation with successive slips while the foreshocks to slip events of WGRN05 were centered approximately at the same point. We observed an evolution of the AE densities of WGRN05 to a broader spatial distribution so that larger parts of the fault plane were covered by high AE activity while individual spots with high densities contributed less to the total activity (Figure 12). During the first two slips, only one major cluster was active, located towards the center of the

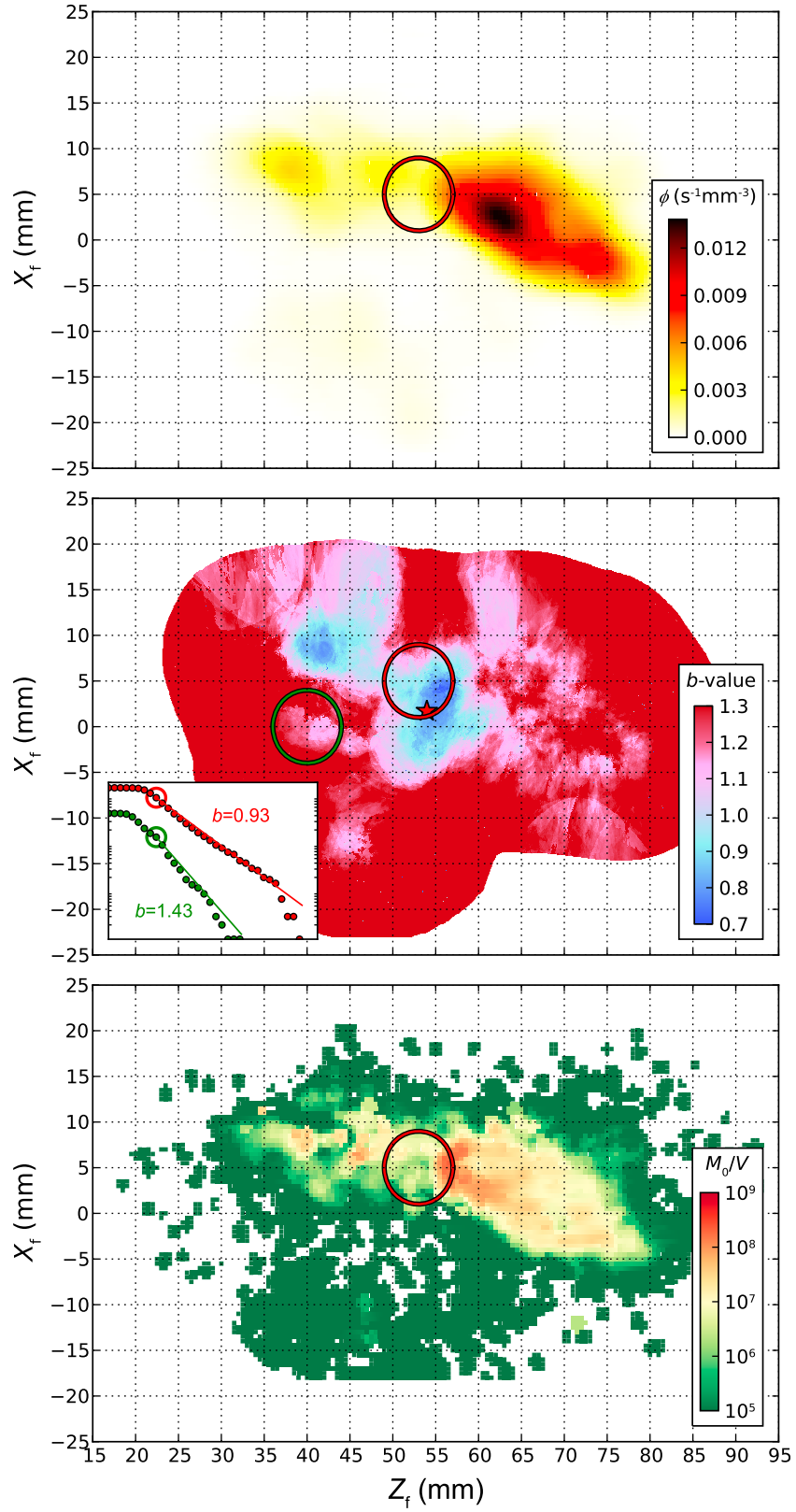


Figure 10. Examples of AE event density (ϕ), b value and moment release maps computed for AEs occurring before slip event 1 of experiment WGRN05. Slip event one (red star) nucleated close to or from within an area of high ϕ , M_0 and low b value. The fmds for high and low b value regions are compared (bottom left in Figure 10 (middle)). The asperity region is connected to low b values, high event density and moment release.

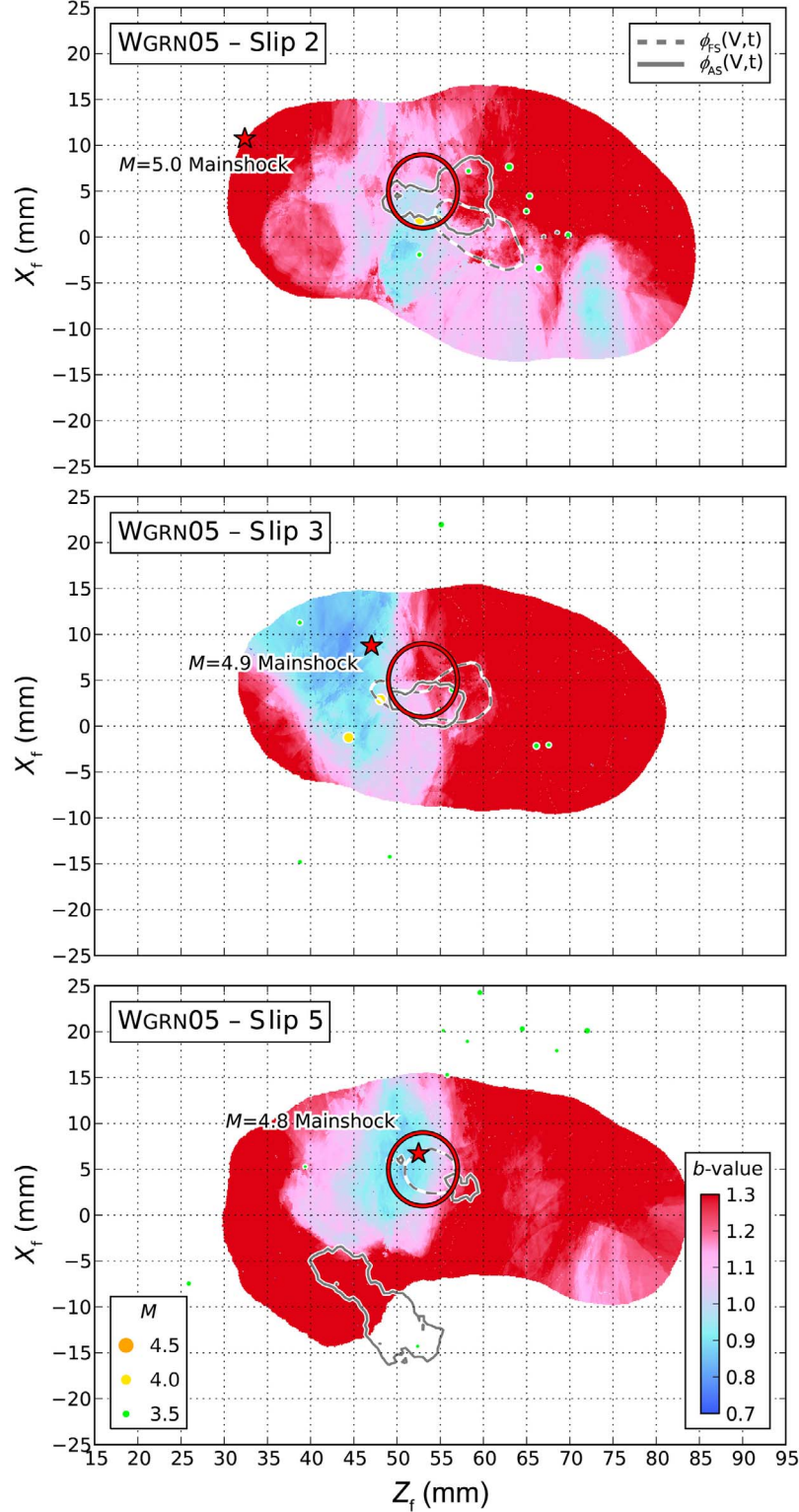


Figure 11. *b* value maps based on foreshocks, contours of foreshock (dashed line) and aftershock (solid black line) densities, hypocenters of 10 largest aftershocks and the main shock nucleation points of slip events 2, 3 and 5 of experiment WGRN05. The size of the aftershocks is indicated by legend at the bottom right. The previously identified asperity region is indicated by the red circle. Low *b* value regions are situated at the border of high AE activity regions of both foreshocks and aftershocks which mark similar regions for the first three preslip periods and are deviating significantly for events 4–6.

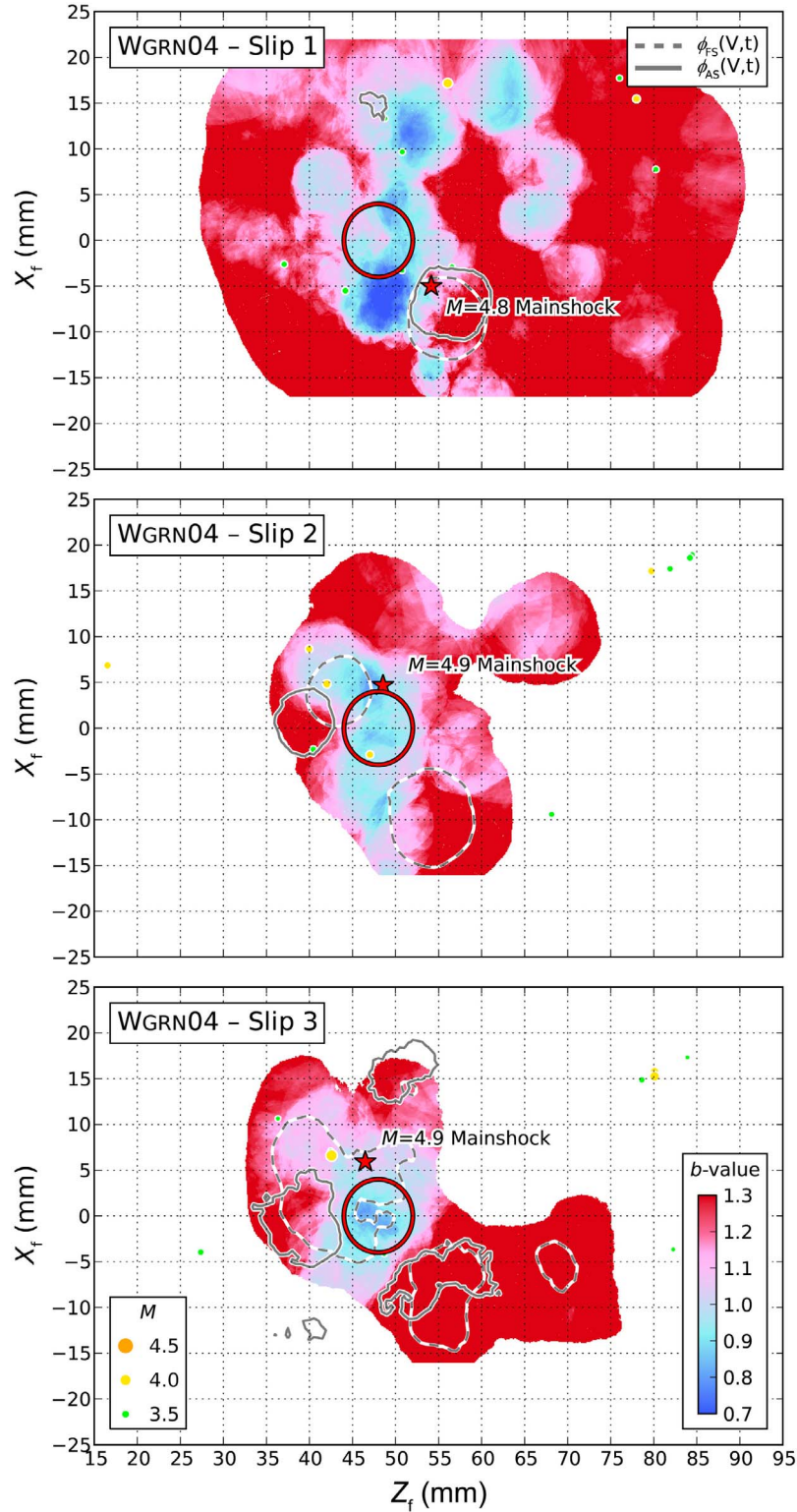


Figure 12. *b* value, foreshock and aftershock densities, main and largest aftershock locations plotted similarly to Figure 11 but now for three different slip events of experiment WGRN04. A combination of *b* value maps, AE event densities and foreshock locations enables the identification of an asperity region (red circle) which is also the nucleation spot of macroscopic slip events.

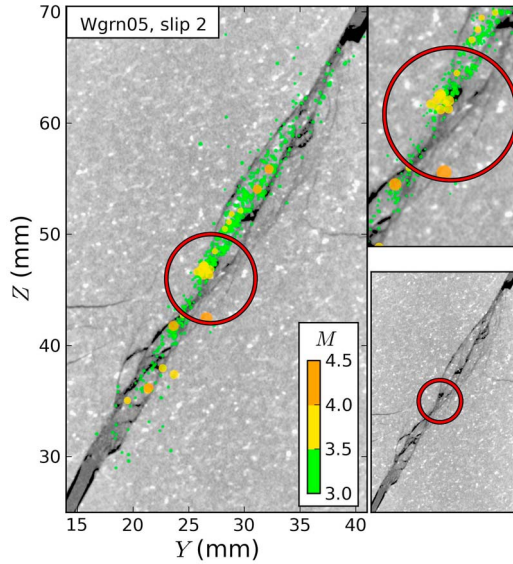


Figure 13. CT scan of central part of sample obtained after the experiments and AE hypocenters (colored dots) for the stick periods before slip event 2 of WGRN05. The colors of hypocenter locations correspond to their magnitudes. The red circle highlights the likely site of a large asperity which was centered at [27,45].

sample. With each successive slip, the AE activity became more distributed and separate clusters were formed. The gradual increase in activity in different fault areas indicates a smoothing process, resulting in a distributed set of small-scale asperities that carried the load and contributed to the AE activity. This process was most visible for slip events 1 to 3 of WGRN04.

[36] To compare information of AE locations with post-experimental fault microstructure, we superimposed AE hypocenters on the CT images of WGRN05. We show results for two exemplary slip events (slip event 2 and 5) of WGRN05. Figure 13 shows the foreshocks of slip event 2 colored with magnitude. AE hypocenter locations follow the larger-scale fault structure. Most AEs could be linked to specific cracks. The uncertainty in hypocenter determination of 3 mm lead to a slightly larger spread of AEs compared to the discrete microcrack traces of the CT images. The demonstrated fault structure is a compilation of many fracture and slip events while the AEs were taken from a narrow zone corresponding to the CT slice during one specific time window only. These effects explain the differences between fault structure and AE locations.

[37] Several large foreshocks (yellow and orange dots) nucleated in fault proximity on larger-scale flaws. Less AE activity was observed close to the notches and away from the fault plane. Several AE clusters were distributed along the fault, perhaps caused by small-scale fault heterogeneities. The previous area of high foreshock activity contrast was also observed on the fault plane at [26, 45], highlighted by a red circle in Figure 13. Three larger foreshocks (at [27, 43], [25, 43], [24.5, 43.5]) occurred just below this region and a dense cluster of large amplitude events above it occurred at [27.5, 47]. The spatial “gap” in AE activity coincided with an area of narrow fault zone, visible in the CT images. The

other parts of the fault zone were wider, consisting of a gouge layer between many small and large cracks. The change from larger fault zone width and multiple fault planes to a narrow zone could be responsible for the enhancement of micro-cracking and seismicity in this area.

[38] Figure 14 shows a superposition of the CT scan and foreshocks prior to slip event 5. The overall seismic activity was smaller and more localized than before slip event 2. We observed several large foreshocks which predominantly nucleated within or close to the asperity region. The main shock originated on the fault plane within the asperity. High activity inside the asperity and large-magnitude events can be connected to continuous fracture or grinding of the previously identified asperity region leading up to slip event 5. The combination of seismic and fault structural information revealed that the region of low b , high seismic moment, and high AE event density was connected to an anomalously thin part of the fault zone. Asperity regions were characterized by small fault zone width, without anastomosing cracks and possibly bare rock surfaces that were in contact and caused the fault to be locked in this region.

4. Discussion

[39] Within the scope of the described experiments, we found some compelling similarities between microseismicity occurrences during sliding of fracture surfaces and crustal seismicity: (1) Laboratory AE records can be separated into foreshocks, main shocks, and aftershocks based on their origin times, rates, and magnitudes. We observed a comparatively low rate during foreshock periods that accelerated almost instantaneously during main shock occurrence which is usually the largest magnitude AE of the sequence. (2) The aftershock rate decay after macroscopic slip can be described by the Omori-Utsu law. (3) The frequency-magnitude distribution of microseismicity in our experiments followed a

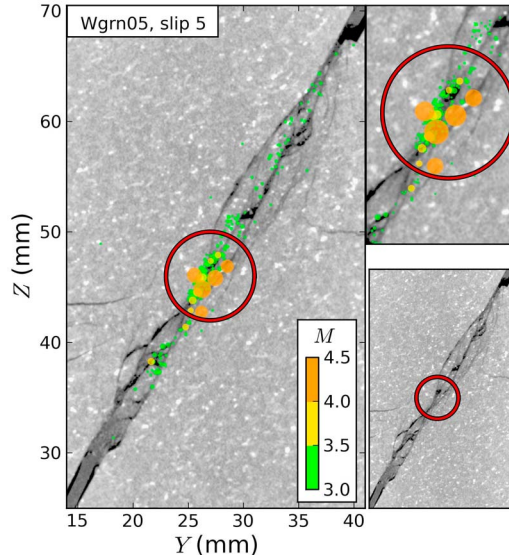


Figure 14. CT scan and AE hypocenters colored according to magnitude for foreshocks to slip event 5 of WGRN05. Most of the AE activity is concentrated within the asperity region indicated by a red circle.

Gutenberg-Richter distribution with an average value of $b \approx 1.1$ and a range between 0.7 and 1.3, which is similar to values observed for earthquake catalogs. b values were higher for aftershock sequences than for foreshocks which is in agreement with *Weeks et al.* [1978]. (4) Similarly to studies conducted on natural seismicity, we performed a detailed b value mapping based on AEs that occurred before macroscopic slip events. The spatial mapping revealed a connection between asperity regions and areas of low b values. This connection has also been observed for areas of increased fault strength within the continental crust [*Wiemer and Wyss*, 1997; *Wyss et al.*, 2000; *Schorlemmer and Wiemer*, 2005]. The spatial variations of b values before slip onsets seem to be a promising tool for the characterization of fault heterogeneity. Absolute b values cannot be meaningfully compared between laboratory experiments and real earthquakes (or even between different earthquake catalogs) because they depend partly on magnitude definitions.

[40] We observed higher AE foreshock densities and high moment release associated with asperity regions. Slip events nucleated in the proximity or from within asperity regions, coinciding with areas of low foreshock b value. A precise estimate of size and location of asperities was limited by the spatial resolution of b value maps. The analysis of foreshock hypocenter distributions demonstrated that large events occurred preferably at the boundaries of asperity regions. Both low and high foreshock activity regions are found within or close to asperity regions forming a distinguishable contrast which was not observed in other areas of the fault.

[41] The foreshock densities changed abruptly close to the asperity region before most of the macroscopic slips. Slip event 5 of WGRN05 resembled an exception in that most of the activity was focused within the asperity region prior to slip. This event was connected to low postrupture strength and the largest stress drop. Slip event 6 again was preceded by the same characteristics of low b , high AE density at asperity edges, and higher moment release. This indicates that the geometric asperity remained largely stationary within the amount of applied displacement despite of high AE activity close by and many slip events which nucleated in its proximity.

[42] In the absence of large, geometric heterogeneity, for example, during fracture experiments of homogeneous rock samples, stress concentrations identified by AE clusters are usually localized at the outer sample surface [*Lockner et al.*, 1991]. During our experiments we did not observe AE clustering at the sample boundaries or in proximity to the tips of the notches, but rather AEs appeared to localize close to the fault and clustered in certain areas on the fault plane. The fact that AE activity occurred localized within a zone of high damage is also connected to a lack of a characteristic length scale of AEs. Both AE-based FMDs and b values, computed from events within a volume close to the fault surface, did not show a preferred AE magnitude. The region around the fault axis was dominated by high damage, i.e. crushed grains and high microcrack densities as a result of a series of stick-slip events. Initial grain size distributions were unlikely to have had a significant influence on micro cracking and AE magnitudes after several slip events and sample fracture. This supports our interpretation that fault plane asperities were one main factor in controlling the locations and size of AEs.

[43] Our experiments provide the possibility to monitor the evolution of a natural fracture surface to a fault zone that contains a gouge layer, a damage zone, and the intact host rock. The largely persistent asperity regions were closely connected to the creation of macroscopic slip events. The faults of both experiments, WGRN04 and WGRN05, showed evidence of smoothing with successive slip events which could be recognized by more distributed microseismicity occurrences and lower residual stresses after slip events.

[44] We observed a set of small and large slip events with various stress drops. Slip events within one experiment had the potential to grow both small or large at similar bulk stresses. This indicates that additionally to far field stress levels local stress field perturbations as a result of geometric fault heterogeneity seem to have a large influence on slip event size, stress drop, and duration. Large slip events were connected to differential stress drops between 130–370 MPa, corresponding to a drop in shear stress between 57 and 160 MPa. The small slip events had a maximum differential stress drop of ~40 MPa. Slip events could be separated into small stress drop events with long duration and large stress drop events that had short slip durations ($\Delta t \leq 0.1$ s). This difference could possibly be used to evaluate if slip events are likely to grow to large sizes before the rupture actually stops. Stress drops of slip events with short durations were larger than for mining-induced seismicity which exhibits shear stress drops of up to 70 MPa [*McGarr et al.*, 1979]. A true comparison between natural and laboratory stress drops is limited because of the large influence of the loading frame stiffness on lab results [*Brace and Byerlee*, 1966].

[45] One major difference between our stick-slip events and natural seismicity is that none of the macroscopic slips were contained within the fault surface but rather caused slip along the entire fault. In contrast to strike-slip earthquakes, which usually nucleate and stop within the fault zone, the end of our ruptures were limited by the sample dimensions and would otherwise extend further. This poses a problem on the estimation of earthquake-equivalent seismic moment and rupture area for our laboratory slip events, and could partially be responsible for high stress drops.

[46] Even though we found many similarities between AE statistics and those of crustal seismicity, the majority of AE source types differ from crustal earthquakes. AE moment tensors usually contain large isotropic components. These could be a result of micromechanical processes only observable at lab scales, for example, damage and surface creation due to tensile cracking and grain fracture. Despite the deviations of AE sources at the smallest scale, some of the larger magnitude AE events can be modeled as double couple sources [*Zang et al.*, 1998; *Thompson et al.*, 2009].

5. Conclusions

[47] We conducted triaxial compression experiments on three Westerly granite samples with and without notches and recorded mechanical and seismic data throughout each experiment. During triaxial loading of the previously created faults, several macroscopic slip events occurred with small and large stress drops. Larger slip events had shorter slip duration with increasing stress drops which could possibly be used to determine the size of a rupture before it actually

stopped. The two experiments on notched rock specimens (WGRN04, WGRN05) produced a series of nine stick-slip events. Eight out of these nine events nucleated within areas of high foreshock moment release, AE event density, and low b value. We demonstrated similarities between microseismicity connected to stick-slips and natural seismicity. An asperity region was identified in CT scan images of specimen WGRN05 by anomalously thin fault zone width. The asperity definition based on AE data coincided with the same area. The overall AE distribution indicates a fault smoothing process after several stick-slips as a result of the failure of large asperities which probably led to a broader distribution of the stress on many load bearing asperities.

[48] Larger scale asperities which approach their critical strength are connected to locally more abundant high amplitude AE events and to the nucleation spots of large slips. Highly stressed asperities cause events to grow larger once they nucleate, providing an explanation for relatively lower b values. The regions of spatial seismicity anomalies show the same characteristics during several stick-slip sequences, indicating the persistence of fault-plane heterogeneity over extended periods. We note a similarity between the current laboratory findings and seismicity based asperity characterization at the San Jacinto-Elsinore fault system [Wyss et al., 2000], the Hayward fault in Northern California [Wyss, 2001] and the Parkfield section of the San Andreas fault [Wiemer and Wyss, 1997; Schorlemmer et al., 2004]. These studies showed that crustal scale asperities are connected to low b value anomalies and can influence the nucleation points and slip distribution of large-magnitude earthquakes. High-resolution mapping of b values, seismic moment, event density, and the identification of connected areas with large contrasts in seismic activity could be used to further improve asperity identification based on natural seismicity.

[49] **Acknowledgments.** We would like to thank David Lockner, an anonymous reviewer and the associate editor for their helpful comments on an earlier version of this manuscript. We also thank Tobias Meier and Andreas Reinicke for animated discussions and for their assistance with conducting the experiments at GFZ-Potsdam. We are grateful for excellent rock sample preparation by Stefan Gehrmann and Matthias Kreplin. We want to thank the open-source community for the Linux operating system and the many programs used in this study (Inkscape, Gimp, Python). This research was supported in part by the Southern Californian Earthquake Center under contribution 11017.

References

- Aki, K. (1965), Maximum likelihood estimate of b in the formula $\log N = a - b \cdot M$ and its confidence limits, *Bull. Earthquake Res. Inst. Univ. Tokyo*, 43, 237–239.
- Aki, K. (1979), Characterization of barriers on an earthquake fault, *J. Geophys. Res.*, 84, 6140–6148.
- Aki, K. (1984), Asperities, barriers, characteristic earthquakes and strong motion prediction, *J. Geophys. Res.*, 89, 5867–5872.
- Amitrano, D. (2003), Brittle-ductile transition and associated seismicity: Experimental and numerical studies and relationship with the b value, *J. Geophys. Res.*, 108(B1), 2044, doi:10.1029/2001JB000680.
- Amitrano, D., and J. Schmittbuhl (2002), Fracture roughness and gouge distribution of a granite shear band, *J. Geophys. Res.*, 107(B12), 2375, doi:10.1029/2002JB001761.
- Ben-Zion, Y., and C. G. Sammis (2003), Characterization of fault zones, *Pure Appl. Geophys.*, 160, 677–715.
- Brace, W. F., and J. D. Byerlee (1966), Stick-slip as a mechanism for earthquakes, *Science*, 153, 990–992.
- Chayes, F. (1950), Composition of the granites of Westerly and Bradford, Rhode Island, *Am. J. Sci.*, 248, 378–407.
- Dietrich, J. H. (1978), Time-dependent friction and mechanics of stick-slip, *Pure Appl. Geophys.*, 116, 790–806.
- Dietrich, J. H., and D. E. Smith (2009), Nonplanar faults: Mechanics of slip and off-fault damage, *Pure Appl. Geophys.*, 166, 1799–1815.
- Engelder, J. T. (1974), Microscopic wear grooves on slickensides: Indicators of paleoseismicity, *J. Geophys. Res.*, 79, 4387–4392.
- Guo, Z., and Y. Ogata (1997), Statistical relations between the parameters of aftershocks in time, space, and magnitude, *J. Geophys. Res.*, 102, 2857–2873.
- Gutenberg, B., and C. F. Richter (1944), Frequency of earthquakes in California, *Bull. Seismol. Soc. Am.*, 34, 185–188.
- Jaeger, J. C., and N. G. W. Cook (1979), *Fundamentals of Rock Mechanics*, Chapman and Hall, London.
- Kanamori, H., and G. S. Stewart (1978), Seismological asperity earthquake of February 4, 1976, *J. Geophys. Res.*, 83, 3427–3434.
- Kato, A., T. Miyatake, and N. Hirata (2010), Asperity and barriers of the 2004 Mid-Niigata prefecture earthquake revealed by highly dense seismic observations *Bull. Seismol. Soc. Am.*, 100, 298–306.
- Lei, X. (2003), How do asperities fracture? An experimental study of unbroken asperities, *Earth Planet. Sci. Lett.*, 26, 247–258.
- Lei, X., K. Masuda, O. Nishizawa, L. Jouniaux, L. Liu, W. Ma, T. Satoh, and K. Kusunose (2004), Detailed analysis of acoustic emission activity during catastrophic fracture of faults in rock, *J. Struct. Geol.*, 26, 247–258.
- Lockner, D., J. Byerlee, V. Kuksenko, A. Ponomarev, and A. Sidorin (1991), Quasi-static, fault growth and shear fracture energy in granite, *Nature*, 350, 39–42.
- Main, I. G., P. G. Meredith, and C. Jones (1989), A reinterpretation of the precursory seismic b -value anomaly from fracture mechanics, *Geophys. J. Int.*, 96, 131–138.
- Malin, P. E., S. N. Blakeslee, M. G. Alvarez, and A. J. Martin (1989), Microearthquake imaging of the Parkfield asperity, *Science*, 244, 557–559.
- McGarr, A., S. M. Spottiswoode, and N. C. Gay (1979), Observations relevant to seismic driving stress, stress drop and efficiency, *J. Geophys. Res.*, 84, 2251–2261.
- Meredith, P. G., I. G. Main, and C. Jones (1990), Temporal variations in seismicity during quasi-static and dynamic rock failure, *Tectonophysics*, 175, 249–268.
- Powers, P. M., and T. H. Jordan (2010), Distribution of seismicity across strike-slip faults in California, *J. Geophys. Res.*, 115, B05305, doi:10.1029/2008JB006234.
- Ruina, A. (1983), Slip instability and state variable friction laws, *J. Geophys. Res.*, 88, 10,359–10,370.
- Sammonds, P., and M. Ohnaka (1998), Evolution of microseismicity during frictional sliding, *Geophys. Res. Lett.*, 25, 699–702.
- Scholz, C. H. (1968), The frequency-magnitude relation of microfracturing in rock and its relation to earthquakes, *Bull. Seismol. Soc. Am.*, 58, 399–415.
- Scholz, C. H. (2002), *The Mechanics of Earthquakes and Faulting*, 2nd ed., Cambridge Univ. Press, New York.
- Schorlemmer, D., and S. Wiemer (2005), Microseismicity data forecast rupture area, *Nature*, 434, 1086, doi:10.1038/4341086a.
- Schorlemmer, D., S. Wiemer, and M. Wyss (2004), Earthquake statistics at Parkfield: 1. Stationarity of b -values, *J. Geophys. Res.*, 109, B12307, doi:10.1029/2004JB003234.
- Sobiesiak, M., U. Meyer, S. Schmidt, H.-J. Gotze, and C. M. Krawczyk (2007), Asperity generating upper crustal sources revealed by b value and isostatic residual anomaly grids in the area of Antofagasta, Chile, *J. Geophys. Res.*, 112, B12308, doi:10.1029/2006JB004796.
- Stanchits, S., S. Vinciguerra, and G. Dresen (2006), Ultrasonic velocities, acoustic emission characteristics and crack damage of basalt and granite, *Pure Appl. Geophys.*, 163, 975–994.
- Stesky, R. M. (1978), Mechanisms of high temperature frictional sliding in Westerly granite, *Can. J. Earth Sci.*, 15, 361–375.
- Thompson, B. D., R. P. Young, and D. A. Lockner (2009), Premonitory acoustic emissions and stick-slip in natural and smooth-faulted Westerly granite, *J. Geophys. Res.*, 114, B02205, doi:10.1029/2008JB005753.
- Utsu, T. (1962), On the nature of three Alaskan aftershock sequences of 1957 and 1958, *Bull. Seismol. Soc. Am.*, 52, 279–297.
- Utsu, T. (1965), A method for determining the value of b in a formula $\log n = a - bM$ showing the magnitude frequency for earthquakes, *Geophys. Bull. Hokkaido Univ.*, 13, 99–103.
- Weeks, J., D. Lockner, and J. Byerlee (1978), Change in b -values during movement on cut surfaces in granite, *Bull. Seismol. Soc. Am.*, 68, 333–341.
- Wiemer, S., and M. Wyss (1997), Mapping the frequency-magnitude distribution in asperities: An improved technique to calculate recurrence times?, *J. Geophys. Res.*, 102, 15,115–15,128.

- Wyss, M. (2001), Locked and creeping patches along the Hayward fault, California, *Geophys. Res. Lett.*, 28, 3537–3540.
- Wyss, M., D. Schorlemmer, and S. Wiemer (2000), Mapping asperities by minima of local recurrence time: The San Jacinto-Elsinore fault zones, *J. Geophys. Res.*, 105, 7829–7844.
- Zang, A., F. Wagner, S. Stanchits, G. Dresen, R. Andresen, and M. Haidekker (1998), Source analysis of acoustic emissions in Aue granite cores under symmetric and asymmetric compressive loads, *Geophys. J. Int.*, 135, 1113–1130.
- Zhang, P., D. B. Slemmons, and F. Mao (1991), Geometric pattern, rupture termination and fault segmentation of the Dixie Valley–Pleasant Valley active normal fault system, Nevada, U.S.A., *J. Struct. Geol.*, 13, 165–176.

T. W. Becker, T. H. W. Goebel, C. Sammis, and D. Schorlemmer, Department of Earth Sciences, University of Southern California, 3651 Trousdale Pkwy., Los Angeles, CA 90089, USA. (tgoebel@usc.edu)

G. Dresen and E. Rybacki, Department of Geodynamics and Geomaterials, German Research Centre for Geosciences, Telegrafenberg D429, Potsdam D-14473, Germany.

S. Stanchits, TerraTek A Schlumberger Co., 1935 S. Fremont Dr., Salt Lake City, UT 84104, USA.